ELECTROCHEMISTRY

A Li_2S-based all-solid-state battery with high energy and superior safety

Yuzhao Liu[1], Xiangyu Meng[1], Zhiyu Wang[1]*, Jieshan Qiu[2]*

Safety risks stem from applying extremely reactive alkali metal anodes and/or oxygen-releasing cathodes in flammable liquid electrolytes restrict the practical use of state-of-the-art high-energy batteries. Here, we propose a intrinsically safe solid-state cell chemistry to satisfy both high energy and cell reliability. An all-solid-state rechargeable battery is designed by energetic yet stable multielectron redox reaction between Li_2S cathode and Si anode in robust solid-state polymer electrolyte with fast ionic transport. Such cells can deliver high specific energy of 500 to 800 Wh kg^{-1} for 500 cycles with fast rate response, negligible self-discharge, and good temperature adaptability. Integrating intrinsic safe cell chemistry to robust cell design further guarantees reversible energy storage against extreme abuse of overheating, overcharge, short circuit, and mechanical damage in the air and water. This work may shed fresh insight into bridging the huge gap between high energy and safety of rechargeable cells for feasible applications and recycle.

INTRODUCTION

Recent years have witnessed the prosperity of high-energy rechargeable batteries using alkali metals (e.g., Li, Na, and K) to meet the carbon-neutral energy demands. Alkali metal anodes with ultrahigh capacities and low reduction potentials can boost the cell energy far beyond the existing Li-ion batteries (*1*, *2*). However, they also induce unstable cell chemistry by extremely high reactivity in flammable organic liquid electrolytes (LEs) (*3*). Premature cell failure and safety hazards are triggered by dendrite-induced short circuits, uncontrolled exothermic side reactions of LEs with alkali metals, and LE leaking on cell damage (*4*). These problems would be even worse in commercial cells against oxygen-releasing intercalation cathode (*5*). Fire/explosion hazards of such cells during disassembly also make battery recycling dangerous and difficult, which is rarely recognized, but reduces economic and environmental sustainability. Replacing unstable LEs with nonflammable and robust solid-state electrolytes (SSEs) offers the ultimate solution to cell safety. Nevertheless, the SSEs raise new concerns on poor interfacial compatibility with ductile alkali metal, metal dendrite penetration along cracks/crystal boundaries, and slow ionic transport (*6*, *7*). Upsurging aqueous or alkali metal-free solid-state cells enable high safety at a cost of cell energy due to a lack of high-capacity cathodes and high-voltage stable water-based electrolytes (*8*, *9*).

Exploring mild yet energetic redox chemistry to bridge the huge gap between high energy and safety of rechargeable batteries is fundamentally important but challenging. As a fully lithiated phase of sulfur (66.7 Li atomic %), lithium sulfide (Li_2S) may meet this desire for several merits (*10*): (i) intrinsic safety without the trouble of highly reactive Li metal and oxygen-releasing cathodes; (ii) unbeatable capacity (1166 mAh g^{-1}) to intercalation-type cathodes; (iii) high compatibility with available high-capacity anodes (e.g., Si) for acquiring high energy density (1550 Wh kg^{-1}); (iv) negligible volume expansion of pre-lithiated structure for meeting thick electrode and solid-state design; (v) superior thermal stability (melting point, 938°C) to sulfur (112.8°C) against overheating; and (vi) low self-discharge enabled by natural activation potential barrier and insolubility in organic electrolyte. These benefits make the Li_2S cathodes naturally suitable for engineering powerful rechargeable cells with intrinsic safety. Pioneer work by Cui *et al.* (*11*) demonstrated the feasibility of high-energy rechargeable cells using Li_2S cathode and Si anode. Afterward, continuous efforts have been devoted to improving the electrochemical activity and stability of Li_2S and Si electrodes by nanostructuring, electrocatalysis, interfacial engineering, tailoring the electrolyte and/or cell configuration, etc. (*12*, *13*). Other types of anode materials such as graphite, Sn, and metal oxides were also used to pair with Li_2S cathode for acquiring high energy without involving Li metal anode (*14*–*16*). Nevertheless, the operating performance and safety of existing Li_2S-based full cells are still far from satisfactory due to a lack of highly active Li_2S cathode, stable high-capacity anode, and the use of highly flammable LEs.

Usually, Li_2S cathodes undergo a similar redox pathway with sulfur cathode in Li-S batteries, where soluble Li polysulfides (LiPS) with various chain lengths act as the redox intermediates to oxidize the Li_2S to sulfur upon charge and vice versa (*17*). In this process, the reversibility of Li_2S cathode and the cells is deteriorated by LiPS leaking into LEs and their shuttling to contaminate the anode (*18*). Various efforts including physical trapping, chemical adsorption, electrocatalysis, and applying electrolyte additives or gel electrolytes have been devoted to reducing LiPS diffusion in working cells (*19*–*24*). Nevertheless, high solubility of LiPS in LEs and gel electrolytes makes it hard to fully eliminate these difficulties. Using LiPS-impermeable SSEs offers an ultimate solution to LiPS problem in Li-S cells (*25*). But they perform poorly for insulating Li_2S with robust ionic lattice and rather poor redox activity even in LEs (*26*). Solid-state polymer electrolytes (SPEs) are superior to inorganic SSEs in interfacial properties and manufacturing feasibility while outperforming LEs in electrochemical stability and reliability (*27*). Recently, the shortcomings in ionic conductivity and interfacial resistance were also addressed by liquid polymerization to SPE (*28*). Applying LiPS-impermeable SPE with fast ionic transport to Li_2S cathodes provides the feasibility of engineering energetic solid-state

[1]State Key Lab of Fine Chemicals, Liaoning Key Lab for Energy Materials and Chemical Engineering, PSU-DUT Joint Center for Energy Research, School of Chemical Engineering, Dalian University of Technology, Dalian 116024, China. [2]College of Chemical Engineering, Beijing University of Chemical Technology, Beijing 100029, China.
*Corresponding author. Email: zywang@dlut.edu.cn (Z.W.); jqiu@dlut.edu.cn (J.Q.)

battery with intrinsic safety, which, however, has not been realized by far.

In this work, we report to achieving both high cell energy and safety in an all-solid-state cell in terms of energetic yet mild multiple-electron redox chemistry between Li_2S cathode and Si anode in SPE (Fig. 1). A multilevel nanoreactor design of the electrode is developed to boost the redox activity of Li_2S cathode while strengthening Si anode in SPE with much stringent requirements on electrode activity and stability than liquid or quasi–solid-state ones. Meanwhile, Li^+ accessibility to both electrodes and cell reversibility are maximized by in situ formation of LiPS-impermeable SPE with fast ionic transport and intimate interfacial contact. Stable and energetic solid-state cell chemistry ensures not only high energy with long cell life and negligible self-discharge but also reversible energy storage against extreme thermal, electrical, and mechanical abuse in the air and water.

RESULTS

Design and structure of Li_2S-based cathode

Polymer fabric is first made by coaxial electrospinning using polymethyl methacrylate (PMMA) containing zeolitic imidazolate framework-67 (ZIF-67) as a core solution and $Ti_3C_2T_x$ MXene dispersed in polyacrylonitrile (PAN) as a sheath fluid (fig. S1). Upon spinning, the shear force of viscous PAN fluid assembles the MXene to hollow nanofibers (MHF) with a shell thickness of 20 to 40 nm (Fig. 2A). The core fibers are converted to Co nanoparticle–decorated carbon nanocages (Co-C) within closely packed MXene shells (denoted as Co-C@MHF) by annealing polymer fabric in H_2/Ar flow (Fig. 2B). It creates a multilevel nanoreactor (Co-C@MHF) for trapping LiPS without restricting their conversion kinetics (Fig. 2, B and C). Transmission electron microscopy (TEM) analysis reveals uniform dispersion of Co nanoparticles with tiny size of several nanometers on metal-organic frameworks (MOF)-derived Co-C nanocages within Co-C@MHF (fig. S2). High-resolution TEM (HRTEM) images further reveal single crystalline nature of Co and the presence of $Ti_3C_2T_x$ MXene with an interlayer spacing of 1.31 nm (Fig. 2C). X-ray powder diffraction (XRD) reveals the presence of face-centered cubic (fcc) Co (JCPDS no. 15-0806) and MXene in such structure (Fig. 2D). Formation of metallic Co (Co^0) is further validated by a $2p_{1/2}/2p_{3/2}$ doublet at 793.6/778.5 eV in Co 2p spectrum of x-ray photoelectron spectroscopy (XPS) (Fig. 2E and fig. S3) (*29*). The $Ti_3C_2T_x$ MXene is revealed by four pairs of $2p_{1/2}/2p_{3/2}$ doublets for Ti-C (455.1/460.8 eV), Ti^{2+} (456.4/462.1 eV), Ti^{3+} (458.1/463.8 eV), and Ti-O (458.8/464.5 eV) in Ti 2p spectrum (Fig. 2F and fig. S3). The weight ratio of MXene and Co is ca. 55.27 and 23.9 weight % (wt %) in Co-C@MHF, respectively. Gaseous sulfur is infiltrated into Co-C@MHF and reacts with Li naphthalenide to generate Li_2S nanocrystallites of several nanometers (Fig. 2, G and H) (*13*). During this process, chemical interactions between surface atoms of Co and electron-donating sites (e.g., N dopant) on the surrounding carbon matrix may help to stabilize the Co metal nanoparticles in Co-C@MHF against conversion to sulfides. This improvement is validated by pronounced XRD peaks from fcc Co (fig. S4A) and the $2p_{3/2}/2p_{1/2}$ doublet at 778.5/793.6 eV for Co^0 in Co 2p XPS spectrum (fig. S5). The sulfur content in S@Co-C@MHF is estimated to ca. 57 wt % on average by the thermogravimetric analysis (TGA) (fig. S6). Complete conversion of sulfur to Li_2S on Co-C@MHF is indicated by no residue of sulfur signals in XRD pattern (fig. S4A) and negligible weight loss of Li_2S@Co-C@MHF upon heating (fig. S4B). Elemental mapping and elemental analysis visualize the uniform dispersion of ca. 65 wt % Li_2S on Co-C@MHF (Li_2S@Co-C@MHF) (Fig. 2I). Such a Li_2S loading level is sufficient for making high-energy batteries considering the absence of heavy metal current collectors and inactive binders.

Half-cell performance of Li_2S-based cathode

Intrinsic performance of Li_2S@Co-C@MHF cathode is first evaluated against Li metal anode in LEs. All the voltages refer to Li/Li^+ in half

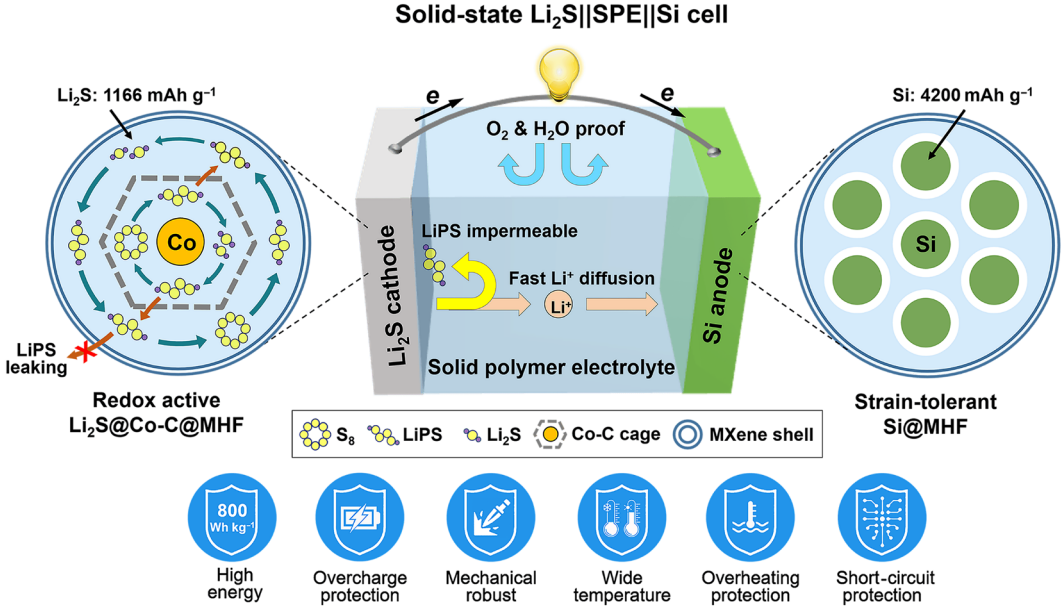

Fig. 1. Schematic illustration of solid-state Li_2S||SPE||Si full cells. The cells satisfy both high energy and reliability by mild multielectron redox chemistry between Li_2S-based cathode with multilevel nanoreactor design and Si anode in robust SPE with high Li^+ conductivity but LiPS, oxygen, and water impermeability.

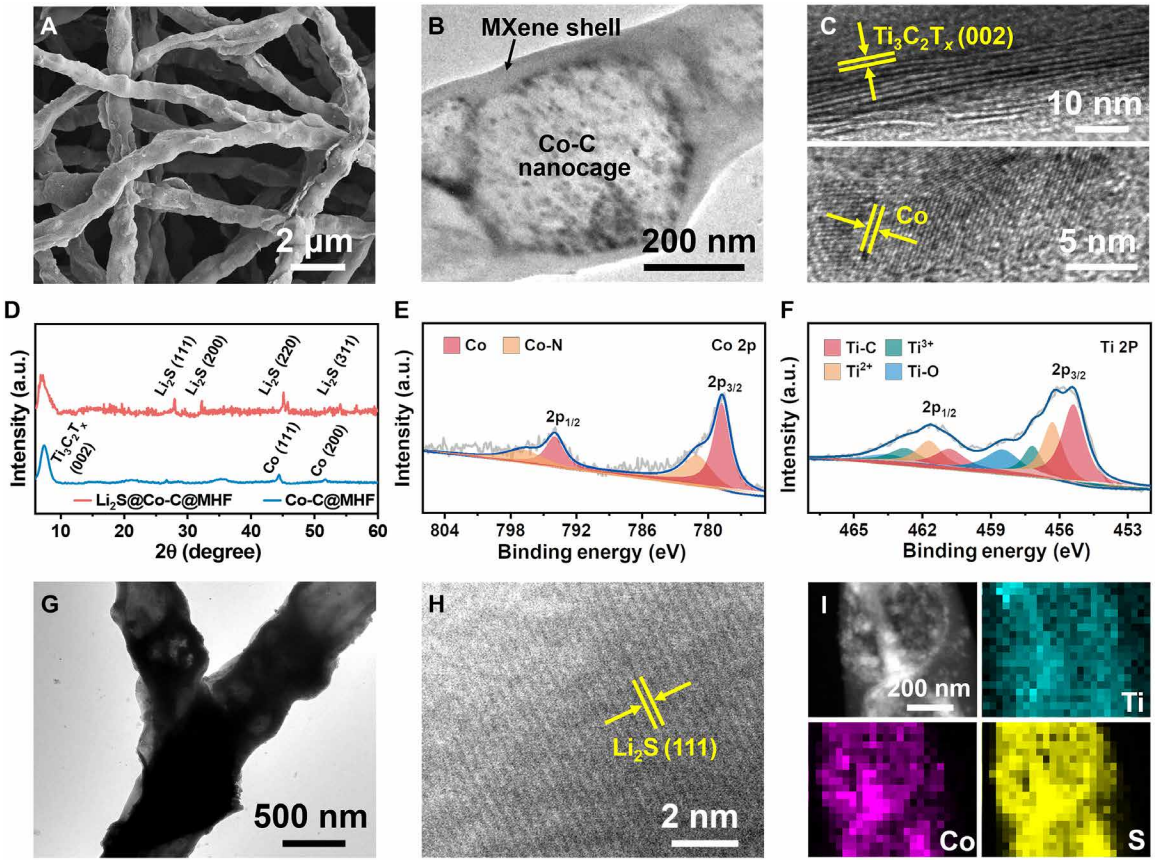

Fig. 2. Characterization of Li_2S-based cathode. (**A**) SEM image of Co-C@MHF fabrics. (**B**) TEM image of a Co-C nanocage within MXene shells. (**C**) HRTEM images of MXene shells (top) and Co nanoparticles (bottom) in Co-C cages. (**D**) XRD patterns of Co-C@MHF and Li_2S@Co-C@MHF. (**E**) Co 2p and (**F**) Ti 2p XPS spectra of Co-C@MHF. a.u., arbitrary units. (**G**) TEM image of Li_2S@Co-C@MHF cathode. (**H**) HRTEM image of Li_2S nanocrystallites in this cathode. (**I**) Element mapping of Li_2S@Co-C@MHF cathode.

cells. Upon initial charge, it requires a low voltage of 2.32 V to activate solid-state Li_2S, followed by LiPS conversion to sulfur via a long and flat plateau around 2.33 to 2.34 V (Fig. 3A). Such an activation potential barrier is far lower than that of bulk Li_2S (3.4 V), most reported nanostructured Li_2S cathodes and even close to the thermodynamic oxidation potential of Li_2S (ca. 2.3 V) (Fig. 3, A and B) (*10*, *26*, *30*–*37*). It suggests that the nanosize effect plays an important but not sole role in activating Li_2S@Co-C@MHF cathode with ease. To uncover the active phase, controlled cathodes including Co-free Li_2S@MHF, MXene-free Li_2S@Co-C@CHF (CHF refers to carbon hollow nanofiber), and MXene/Co-free Li_2S@CHF are tested under identical conditions (Fig. 3A and fig. S7). It seems that the presence of Co is more effective at reducing Li_2S activation potential, while MXene hollow structure works better in accumulating LiPS to propel their conversion to sulfur forward (Fig. 3A). Overall, both cathodes show much lower Li_2S activation and charge potential relative to bulk Li_2S and Li_2S@CHF, which, however, is still far inferior to Li_2S@Co-C@MHF. Such a comparison highlights the critical role of MHF and Co-C cages in enhancing the redox activity of Li_2S cathode.

Effectiveness of Co-C@MHF nanoreactors in catalyzing LiPS conversion is revealed by cyclic voltammetry (CV) analysis of symmetric cells with Co-C@MHF as identical working and counter electrodes in LE with 0.2 M Li_2S_6. At various scan rates, the Co-C@MHF exhibits symmetric redox peaks with a narrow voltage gap, indicating fast LiPS conversion kinetics with high reversibility (fig. S8, A and B). In contrast, the Co-C@CHF without MXene shells shows asymmetric CVs due to low electrode reversibility by LiPS loss to the electrolyte (fig. S8C). The LiPS conversion in Co-free MHF is highly reversible with low redox currents, showing a low redox efficiency (fig. S8D). These results suggest that a synergy of Co and MHF in multilevel nanoreactor is critical to boosting LiPS conversion in Co-C@MHF.

The Li_2S@Co-C@MHF cathode with Li_2S loading of 2.0 mg cm^{-2} delivers an initial charge capacity of 1070 mAh g^{-1} and when charged to 3.5 V at 0.2 C (1 C = 1166 mAh g^{-1}), corresponding to nearly full utilization of Li_2S (Fig. 3A). The initial Coulombic efficiency (CE) is ca. 83% (fig. S9). After initial activation, it retains a high capacity of 835 mAh g^{-1} with negligible activation overpotential by charging to 2.8 V (Fig. 3C). The discharge curves show two plateaus at ca. 2.3 and 2.1 V for sulfur reduction to long-chain LiPS (Li_2S_x, $6 \leq x \leq 8$) and then short-chain ones (Li_2S_x, $2 < x \leq 4$) and Li_2S, respectively (*22*). This redox behavior is also revealed by CV analysis, where an anodic peak appears at 2.38 V for Li_2S oxidation to sulfur, and two cathodic peaks rise at 2.3 and 2.03 V for sulfur reduction to long-chain LiPS and finally to Li_2S (fig. S10) (*38*). When scanned at higher rates, the redox peaks in CVs remain distinguished with similar shapes and slightly increased voltage gaps.

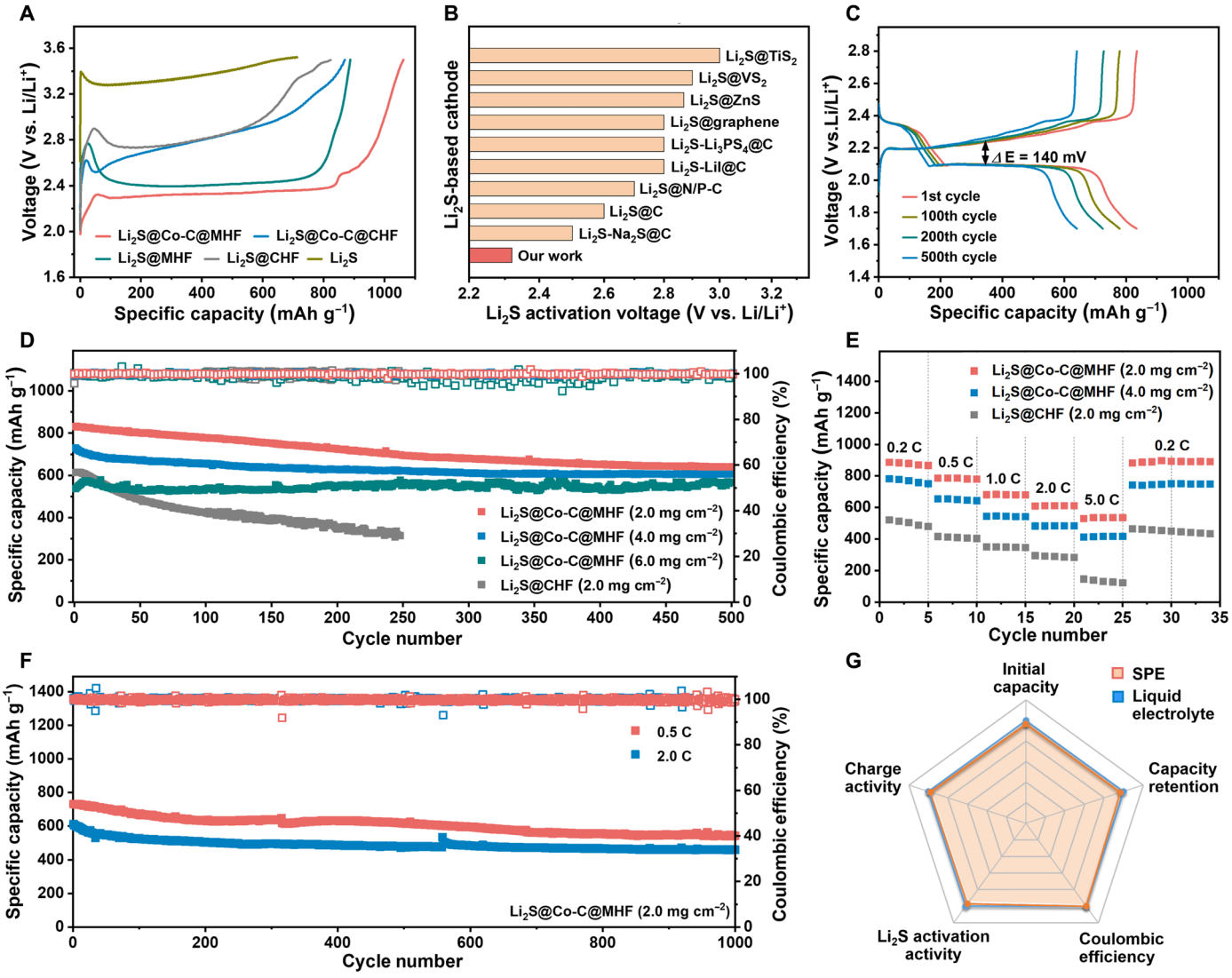

Fig. 3. Performance of Li_2S-based cathode in half cells. (**A**) Charge voltage curves of Li_2S@Co-C@MHF, Li_2S@Co-C@CHF, Li_2S@MHF, Li_2S@CHF, and bulk Li_2S cathodes for initial activation at 0.2 C. (**B**) A comparison of Li_2S@Co-C@MHF and reported Li_2S-based cathodes in the activation potential barrier. (**C**) Discharge-charge voltage curves and (**D**) cycling stability of Li_2S@Co-C@MHF cathodes with different Li_2S loading at 0.2 C. (**E**) Rate capability of Li_2S@Co-C@MHF with various Li_2S loading. (**F**) Cycling stability at higher current rates of 0.5 and 2.0 C. (**G**) A comparison of the performance of this Li_2S-based cathode in LEs and SPE. All the properties in the radar chart are normalized to that in LEs.

It renders high redox activity and fast kinetics of Li_2S@Co-C@MHF cathode. Long-term efficiency of the electrocatalytic effect induces low electrode polarization for 500 cycles with a narrow charge-discharge voltage difference (ΔE = 140 mV). After that, 77% of the initial capacity can be retained with nearly 100% CE at 0.2 C in contrast to fast capacity decay of Li_2S@CHF (Fig. 3D). Positive role of Co-C@MHF nanoreactors in enhancing Li_2S utilization and cathode reversibility is highlighted by superior capacities and cycling stability to Li_2S@Co-C@CHF and Li_2S@MHF (fig. S11). It allows the Li_2S@Co-C@MHF cathode to deliver high capacities of 529 to 785 mAh g^{-1} with low ΔE at high rates of 0.5 to 5.0 C (Fig. 3E and fig. S12). When cycled at 0.5 to 2.0 C, this cathode shows exceptional cycling stability with ultralow capacity decay of 0.024 to 0.027% per cycle for 1000 cycles and nearly 100% CE (Fig. 3F). The improvement in electrode kinetics works effectively for the cathode with doubled (4.0 mg cm^{-2}) or tripled (6.0 mg cm^{-2}) Li_2S loading. They can retain high capacities of 614 to 729 mAh g^{-1} with stable capacity retention of 81 to 83% after 500 cycles at 0.2 C (Fig. 3D). For Li_2S@Co-C@MHF cathode with 4.0 mg cm^{-2} Li_2S loading, high capacities of 410 to 650 mAh g^{-1} can be delivered at high rates of 0.5 to 5.0 C (Fig. 3E).

The performance of Li_2S@Co-C@MHF is further evaluated in SPE against Li metal anode. Ring-opening polymerization of 1,3-dioxolane (DOL) containing lithium bistrifluoromethanesulfonylimide (LiTFSI) is used to in situ–generate the SPE with a high ion conductivity of 2.2×10^{-3} S cm^{-1} and LiPS impermeability around the electrode for optimizing interfacial properties (figs. S13 to S15) (*28*). The $LiNO_3$ is absent in SPE since it can inhibit ring-open reaction and

polymerization of DOL (*39*). Polymerization of DOL to liquid-free solid polymer electrolyte is validated by Fourier transform infrared (FTIR) spectroscopy and Raman analysis. FTIR spectra reveal the polymerization of DOL by several characteristics: (i) the rise of long-chain vibration at ca. 852 cm^{-1}; (ii) a negative shift of C—O—C vibration from ca. 1080 to 1029 cm^{-1} to 994 to 1055 cm^{-1}; and (iii) the C—H out-of-plane vibration from DOL monomer disappears at ca. 915 cm^{-1} (fig. S16) (*28*). Ring opening of DOL is further indicated by the missing of C—O—C ring stretching mode of DOL monomer but the rise of vibration modes from C—O and CH_2 on the linear poly-DOL chains in Raman spectra (fig. S17) (*28*). The TGA also rules out the presence of free volatile solvent in the SPE by negligible weight loss below ca. 120°C (fig. S18). The ionic conductivity of such SPE can be varied in a range of 1.0 to 7.3 mS cm^{-1} between 0° and 80°C, which rises with temperature increasing and can be well described by the Arrhenius model (fig. S19). This result suggests the ionic transport with a rafting process decoupled from the long-range motion of polymer chains (*40*). When charged to 2.8 V, the Li_2S@Co-C@MHF with 2.0 mg cm^{-2} Li_2S loading exhibits a long and flat plateau, delivering a high capacity of 805 mAh g^{-1} in SPE (fig. S20A). Two voltage plateaus still appear at ca. 2.3 and 2.0 V upon discharge, revealing a similar LiPS-intermediated redox pathway with that in LEs. This mechanism is enabled by LiPS dissolution on electrode interface via strong chemical interaction with movable molecular chains of SPE. In SPE, the Li_2S@Co-C@MHF shows increased but not so notable electrode polarization with slightly enlarged ΔE to 165 mV than that in LEs (140 mV) (fig. S20A). A high capacity of 640 mAh g^{-1} is achieved with stable capacity retention of 79 and 99.5% CE after 300 cycles at 0.2 C (fig. S20B). Overall, the excellent performance of Li_2S@Co-C@MHF cathode can be kept in SPE in terms of efficient Li_2S utilization, high redox activity, and good reversibility (Fig. 3G).

Fabrication and half-cell performance of Si-based anode

The Si is a very promising anode material because of its ultrahigh theoretical capacity (4200 mAh g^{-1}) and low discharge potential. However, the Si anodes generally encounter a short lifetime due to severe electrode pulverization caused by huge volume expansion (~300%) upon Li uptaking. The $Ti_3C_2T_x$ MXene with metallic conductivity (ca. 5600 S cm^{-1}) and high elastic modulus (330 ± 30 GPa) is used to strengthen the Si anode (*41*). Free-standing Si anode with 70 wt % Si is made by filling Si nanoparticles with a small size of 30 to 50 nm into MXene hollow nanofibers (Si@MHF) via coaxial electrospinning (fig. S21). Such anode with Si loading of 2.0 mg cm^{-2} delivers a high capacity of 1266 mAh g^{-1} and good capacity retention of 84% after 200 cycles at a current density of 0.2 A g^{-1} in ether-based LE (fig. S22A). The discharge voltage plateau is as low as 0.17 V (fig. S22B). Robust MHF with ample free room and high conductivity can effectively prevent the Si anode from failure by volume change–induced strain and electrical isolation upon Li uptaking. It enables excellent robustness against repeated cycling at high rates of 0.2 to 5.0 A g^{-1} for acquiring high capacities of 770 to 1500 mAh g^{-1} with more than 98% CE (fig. S22C). At a high rate of 2.0 A g^{-1}, the Si@MHF anode can work steadily for 500 cycles to deliver a capacity of 590 mAh g^{-1} with a low capacity decay of 0.074% per cycle and nearly 100% CE (fig. S22D). Such Si anode with high capacity, excellent stability, and low discharge voltage well matches the demand of engineering high-energy cells with Li_2S cathode.

Assembly and performance of solid-state Li_2S||SPE||Si full cells

Rechargeable solid-state full cells are assembled from Li_2S@Co-C@MHF cathode and Si@MHF anode with an areal capacity ratio of negative to positive electrodes (N/P) ratio of ca. 1.2 in DOL-based SPE (denoted as Li_2S||SPE||Si). The SPE is sufficiently permeated into both electrodes by in situ polymerization for creating a uniform and intimate electrode-electrolyte interface. It is visualized by homogeneous distribution of the F element in the cross section of Li_2S||SPE||Si cells (Fig. 4A). This solid-state cell can operate within a voltage window of 1.2 to 2.8 V (fig. S23). Distinct to inorganic ceramic or sulfide-based SSEs, there are movable molecular chains and abundant highly polar groups in SPE. Their presence allows the accommodation of LiPS at the electrode-SPE interface to enable a LiPS-intermediated cell reaction (Fig. 4B) (*28*, *42*, *43*)

$$\text{Cathode reaction: } x/2\ Li_2S \leftrightarrow x\ LiPS \leftrightarrow x/2S + x\ Li^+ + xe^- \quad (1)$$

$$\text{Anode reaction: } Si + x\ Li^+ + xe^- \leftrightarrow Li_xSi \quad (2)$$

The Li_2S||SPE||Si cells, limited by Li_2S cathode (2.0 mg cm^{-2}), exhibit a high initial CE of 80% (fig. S24). It is very important to secure high energy and reversibility of full cells without excess Li source. After initial activation, it delivers a high capacity of 740 mAh g^{-1} with a stable capacity retention of 87.8% and high CE above 99% for 300 cycles at 0.2 C (1 C = 1166 mAh g^{-1}) (Fig. 4C). A high capacity of 652 mAh g^{-1} can be maintained for 300 cycles with 86% capacity retention and high CE by increasing cathode loading to 4.0 mg cm^{-2} at 0.2 C. At high current rates of 0.5 to 2.0 C, such cells can deliver high capacities of 440 to 654 mAh g^{-1} with more than 99% CE (Fig. 4D and fig. S25). Long life of 500 cycles is achieved with 73% capacity retention and high CE at 0.5 C due to restricted detrimental side reactions (Fig. 4E). The specific energy of such full cells is around 800 Wh $kg^{-1}_{Li2S+Si}$ in terms of total active mass in the cathode and anode. High specific energy of 528 Wh kg^{-1}_{EM} could still be retained if considering the entire mass of both electrodes (EM), which even exceeds most of the reported Li_2S-based full cells using LEs (Fig. 4F) (*11*–*14*, *36*, *44*–*47*). The Li_2S||SPE||Si full cells also deliver superior specific energy and power to reported solid-state cells with different cell principles such as Li||Li_2S, Li||LFP, Li||NMC, Ag-C||NMC, and Zn||MnO_x (Fig. 4G) (*48*–*55*). Soft-packaged Li_2S||SPE||Si pouch cells also exhibit stable energy output and good flexibility with an initial capacity of 647 mAh g^{-1} and more than 97% CE for 50 cycles without electrolyte leaking risk (fig. S26).

This solid-state cell also demonstrates good adaptability to a wide temperature range of −20° to 80°C, where they can well retain the two-step redox behavior (fig. S27). Raising the temperature from −20° to 80°C rapidly rises the cell capacity from 221 to 860 mAh g^{-1} by accelerated electrode kinetics at elevated temperature (Fig. 4H). Whereas the Li-S cells encounter rapid performance decay and even failure at high temperature by aggravated LiPS shuttling and detrimental side reaction between Li metal anode and LEs (*56*). For Li-S cells, infinite LiPS shuttling and their irreversible reactions with Li metal anode not only deteriorate the cell reversibility but also induce serious self-discharge to shorten the storage life (*57*). In contrast, the self-discharge is effectively restricted in Li_2S||SPE||Si full cells, thanks to the use of Li_2S cathode with natural activation potential barrier in LiPS-insoluble SPE. The open-circuit voltage (OCV) of fresh cells can be kept stable with negligible decay

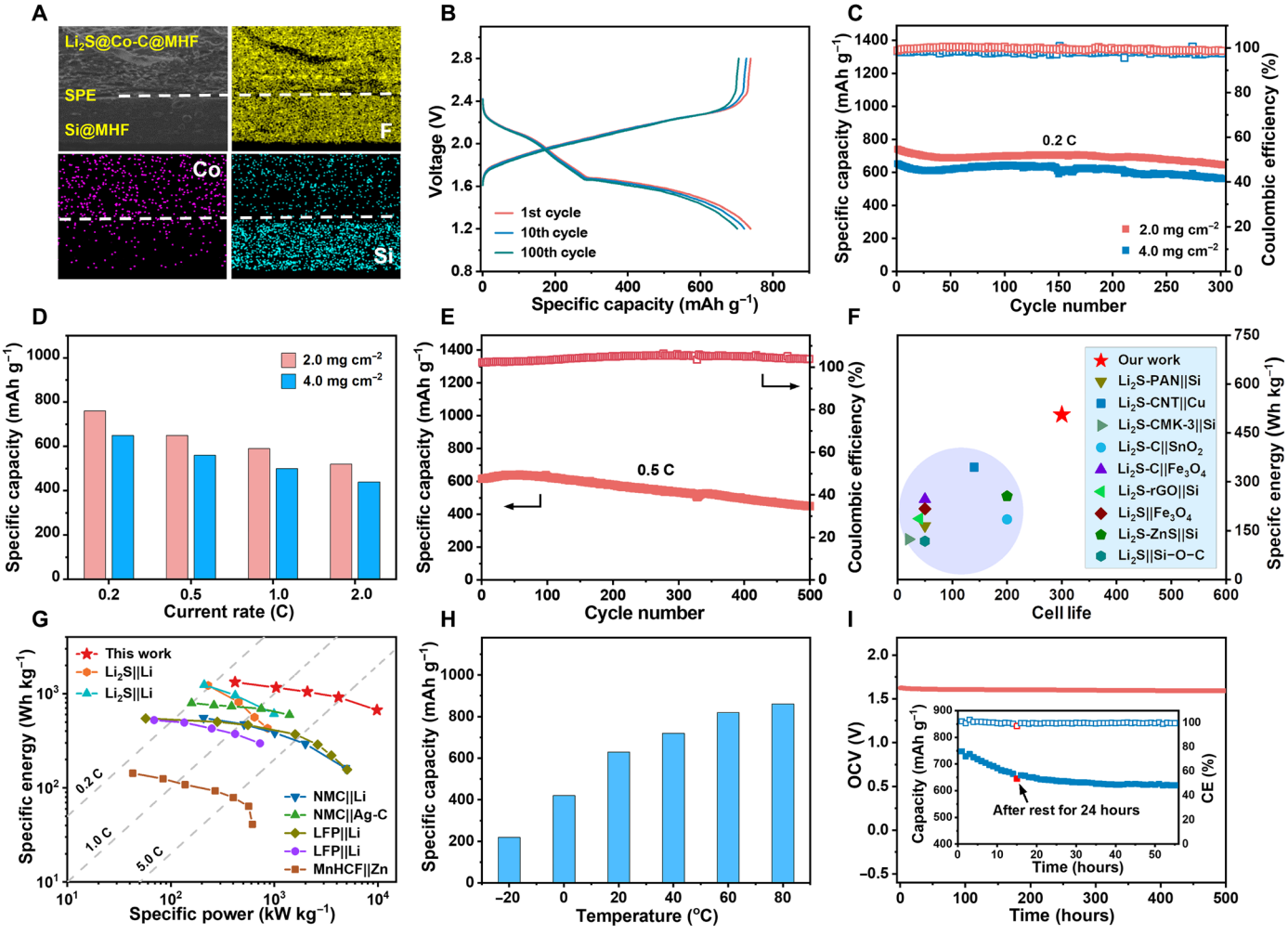

Fig. 4. Performance of solid-state Li_2S||SPE||Si cells. (**A**) Elemental mapping showing the homogeneous distribution of SPE within Li_2S||SPE||Si full cell. (**B**) Discharge-charge voltage curves for different cycles at 0.2 C. (**C**) Cycling stability at 0.2 C and (**D**) rate capability at various current rates for the cells limited by Li_2S cathode with various mass loading. (**E**) Long-term cycling stability and CE at 0.5 C. (**F**) A comparison with reported Li_2S-based full cells in specific energy and cell lifetime. (**G**) Ragone plot of this full cell compared with the performance of reported solid-state cells, where the specific energy and power are calculated by the active mass of the cathode. (**H**) Capacity retention against continuously varied operating temperatures at 0.2 C. (**I**) The OCV stability of fresh cells for 500 hours. The inset is the capacity retention against self-discharge in working cells.

for as long as 500 hours (Fig. 4I). For the cells running after 14 cycles, the capacity is slightly lost by 2.7% after resting for 24 hours but is largely recovered in the next cycle, indicating high effectiveness in suppressing the self-discharge in working cells (the inset in Fig. 4I).

Safety assessment of solid-state Li_2S||SPE||Si full cells

Mild multielectron redox chemistry between Li_2S and Si avoids the trouble of extremely reactive Li metal or oxide electrodes, predetermining high intrinsic safety with less sacrifice of cell energy. Conducting this safe cell chemistry in LiPS, water and oxygen-impermeable SPE with good mechanical robustness and thermal resistance further strengthens the cell reliability under abuse conditions. Thermal-resistant properties of such cells are evaluated by using soft-packaged pouch cells with a single electrode layer to rule out the uncertain effect on the thermal runaway. Upon heating to 100°C, the Li_2S||SPE||Si cells can keep working to power the LEDs without cell deformation (Fig. 5A and fig. S28). Whereas overheating the Li-S cells with similar electrode loading induces large and fast swelling by electrolyte evaporation and decomposition and its vigorous side reactions with Li metal anode (Fig. 5A). During heating, the Li_2S||SPE||Si cells show high thermal resistance with much lower temperatures by 15° to 20°C relative to Li-S cells. High reliability of such cells against electrical abuse is visualized by a negligible thermal runaway from fully charged Li_2S||SPE||Si cells upon external short circuit (middle, Fig. 5B). Nail penetration on charged Li_2S||SPE||Si cells just induces a slight temperature rise around the puncture point (right, Fig. 5B). It is in contrast to the Li-S cells with three to five times temperature rise after external short circuit or nail penetration (Fig. 5C). Replacing SPE with liquid electrolyte in Li_2S||Si cells only induces a slightly higher temperature rise against external short circuit and nail penetration, highlighting the intrinsic high safety of Li_2S||Si cell chemistry (fig. S29).

The DOL-based SPE can resist high voltages up to 5.0 V in contrast to liquid DOL electrolyte that decomposes at 4.2 V (fig. S30). A

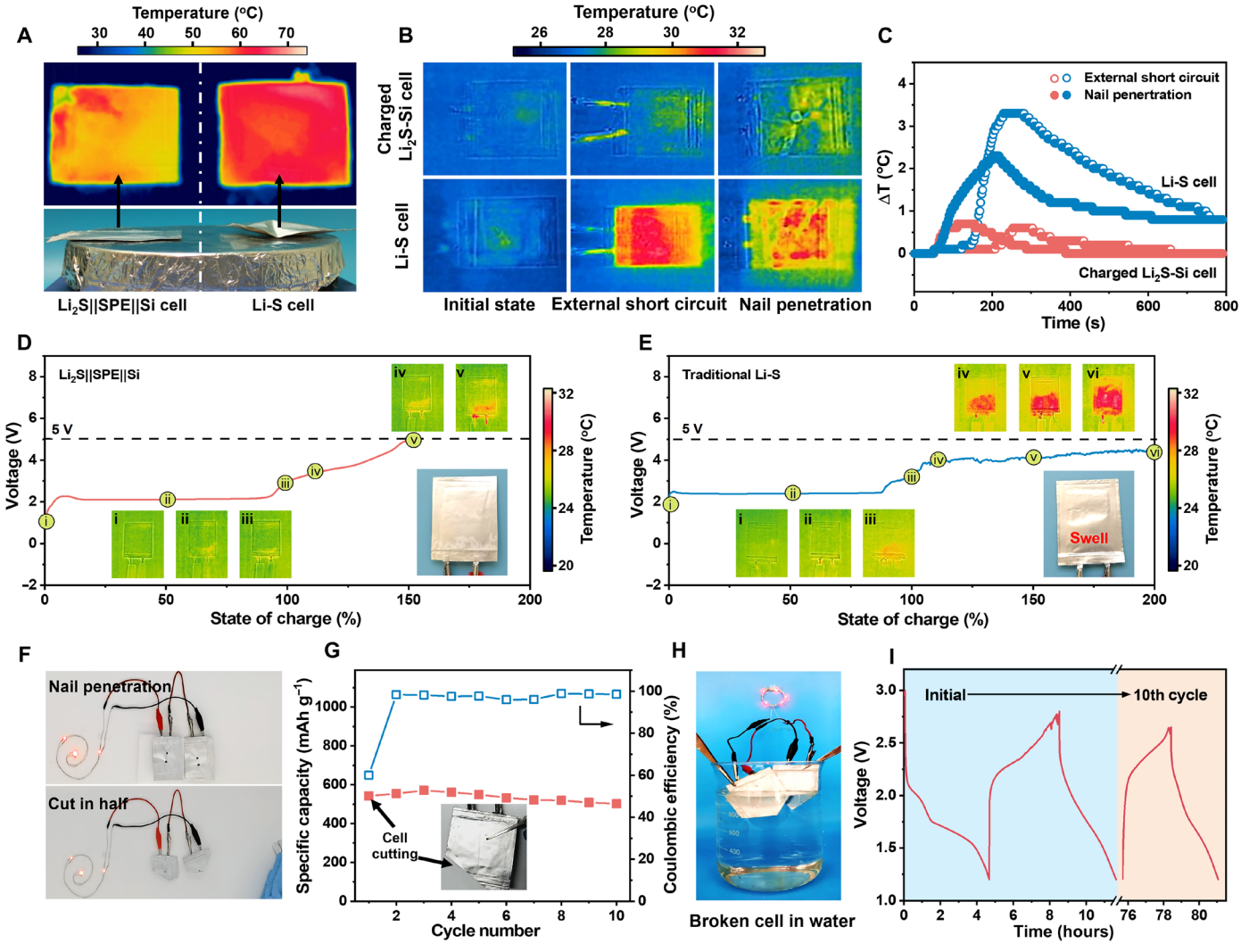

Fig. 5. Safety assessment of solid-state Li_2S||SPE||Si cells. Infrared thermography of a fully charged solid-state cell compared with Li-S battery upon (**A**) overheating, (**B**) external short circuit, and nail penetration. (**C**) Temperature versus time curves of a charged solid-state cell and Li-S battery during external short circuit and nail penetration. Thermal runaway from (**D**) Li_2S||SPE||Si cell and (**E**) Li-S battery during overcharge to 5.0 V. The insets are the infrared thermography of the cells at different depths of charge. (**F**) Optical images of the LEDs powered by solid-state cells after nail penetration (top) and the next cutting in half in the air (bottom). (**G**) Cycling performance and CE of a solid-state cell after cutting a large part in the air. (**H**) Optical image of the broken solid-state cells in water to power the LEDs. (**I**) Corresponding discharge-charge voltage curves of broken cells at the 1st and 10th cycle in water. Photo credit: Yuzhao Liu, Dalian University of Technology.

synergy of stable cell chemistry and such a widened electrochemical stability window works effectively in preventing the cells from damage by overcharge. Charging this solid-state cell to 5.0 V at 1.0 C induces no electrolyte decomposition and cell failure with slight thermal runaway in 152% depth of charge (Fig. 5D). Postmortem scanning electron microscopy (SEM) and XRD analysis reveal that no Li metal plating is on the surface of Si anode after overcharge (fig. S31). This advantage is superior to graphite anode, which suffers from severe Li plating when lithiation capacity exceeds 25% (*58*). After overcharge, the Li_2S||SPE||Si cells can keep cycling normally to deliver high capacities more than 570 to 620 mAh g^{-1} with more than 97% CE (fig. S32A). Whereas the Li-S cells encounter apparent swelling with severe thermal runaway when charge voltage exceeds 4.0 V. Continuous electrolyte decomposition happens to restrict the cell voltage below 4.5 V (Fig. 5E). After 200% charge depth, uneven Li metal stripping and isolation from the anode induce dendrite growth on Li metal anode and separator in Li-S cells (fig. S33), causing cell failure after overcharge (fig. S32B). Such problems would be even worse in a large set of thickly packed cells to cause fire/explosion under abuse conditions.

This solid-state cell also exhibits high reliability against mechanical damage such as nail penetration and severe cutting in the air without SPE leakage and cell failure (Fig. 5F and movies S1 and S2). After cutting a large part in the air, they can maintain reversible energy storage and output with high capacities more than 510 mAh g^{-1}, 93.7% capacity retention, and above 96% CE for 10 cycles at least (Fig. 5G and fig. S34). Further emerging the cells cutting in half into the water causes no violent reactions, cell leaking, and deformation (Fig. 5, H to I, and movie S3). In this case, the broken solid-state Li_2S||SPE||Si cells could even retain stable discharge-charge

behavior for repeated cycles to deliver capacities more than 430 mAh g^{-1} and more than 85% CE (Fig. 5I). Superb safety of such cells against extreme abuse conditions stems from a synergy of stable cell chemistry and robust solid-state configuration with water/oxygen-resistant SPE interweaving into the electrodes. It not only greatly improves the practical reliability but also is important to reduce the cost and risk of battery recycling.

DISCUSSION

Positive effect of Co-C@MHF on Li_2S oxidation kinetics

For Li_2S cathode, the charging process has to overcome high energy barrier of initial activation and next LiPS conversion to sulfur. These reactions are thermodynamically unfavorable and limit the kinetics, efficiency, and reversibility of Li_2S cathode. Given previous studies on LiPS conversion on $Ti_3C_2T_x$ Mxene, we focus on the effect of Co in Co-C@MHF nanoreactors on Li_2S oxidation behavior. First-principle calculation reveals the strong Lewis acid-base interaction between Li_2S or LiPS (Li_2S_4 and Li_2S_6) and electron-donating Co atoms on typical (100), (110), and (111) facets of fcc Co (Fig. 6A and fig. S35). The formation of Co—S bonds is validated by the doublets at 161.3/162.6 and 782.9/789.4 eV in S 2p and Co 2p XPS spectrum of discharged Li_2S@Co-C@MHF cathode, respectively (fig. S36). The Li_2S or LiPS molecules are adsorbed on the Co surface with significant molecular distortion and a high binding energy (E_b) of −1.5 to −13.8 eV by strong chemical interaction (Fig. 6A and fig. S35). Among various facets, the Co (110) plane exhibits the most appropriate absorption of Li_2S and LiPS (Fig. 6B). Efficient LiPS adsorption on Co-C@MHF can be visualized by far lower LiPS residue in the electrolyte exposed to it (fig. S37). This effect is undoubtedly important to inhibiting LiPS leaking for better electrode reversibility. It also induces high LiPS accumulation on electrode interface to supply sufficient redox mediators for dissolving Li_2S with ease (*59*). Strong interaction of Li_2S with the Co surface also effectively weakens the Li—S bonds in robust ionic lattice of Li_2S for easier Li^+ extraction from Li_2S. A rather strong interaction between the Co (100) facet and Li_2S can even spontaneously break the Li_2S cluster without an energy barrier, which is favorable to minimizing the Li_2S activation potential barrier (Fig. 6C).

Highly conductive MXene with "sulfiphilic" surface is known to show dual-mode adsorption of LiPS via Lewis acid-base interaction and thiosulfate formation (*60*). On this basis, the MHF with dense MXene hollow shells provides a highly confined microenvironment with sulfiphilic boundary to prevent the leaking of LiPS escaped from Co-C nanocages inside. Such an effect further enhances the reversibility and redox activity of Li_2S cathode with less sacrifice of LiPS conversion kinetics inside Co-C nanocages. Macroscopically, this improvement can be manifested by the long and flat plateau of MHF-involved Li_2S cathodes upon charge, which is distinct to the sloping curve of the electrode without MXene hollow structure (Fig. 3A). The presence of MHF also contributes greatly to reducing the Li_2S activation potential by 0.3 V relative to MXene-free Co-C@CHF (Fig. 3A). Such enhancement is ascribed to accelerated electrochemical oxidation [$Li_2S_{(s)} + e \rightarrow Li_2S_{x(l)}$] and chemical comproportionation [e.g., $2Li_2S_{8(l)} + 2Li_2S_{(s)} \rightarrow Li_2S_{6(l)} + 3Li_2S_{4(l)}$] of Li_2S in MHF accumulating high LiPS concentration (*17*).

In operando analysis of redox chemistry of Li_2S cathode

The variation of LiPS in species and concentration during discharge-charge process is monitored in working cells by in operando ultraviolet-visible (UV-vis) spectroscopy. It visualizes the high effectiveness of Co-C@MHF nanoreactors in promoting LiPS adsorption and redox conversion in real time of cycling. The LiPS species with various chain lengths including Li_2S_8, Li_2S_6, Li_2S_4, and Li_2S_2 are identified by the maxima of the first-order derivative of UV-vis adsorption at λ = 570, 535, 510, and 470 nm, respectively. The natural logarithm of LiPS concentration is proportional to the spectrum intensity based on Beer-Lambert's law. In LEs, the contour UV-vis pattern reveals the high residue of LiPS with various chain lengths in the cells using MXene and Co-free Li_2S@CHF cathode throughout and after cycling (Fig. 6D). It is a result of sluggish conversion and severe leaking of LiPS into the electrolyte. In contrast, efficient conversion of long-chain to short-chain LiPS reduces LiPS residual level by two to three times in the cells with Li_2S@Co-C@MHF cathode throughout cycling (Fig. 6E). In solid-state cells, LiPS leaking is fully eliminated to induce negligible signals of LiPS for the same cathode throughout the discharge-charge process, which is vital to maximizing the cell reversibility (Fig. 6F).

In operando XRD analysis is performed to monitor the activation and dissociation behavior of Li_2S cathodes in different charge states (Fig. 6G). Activation of Li_2S@Co-C@MHF is triggered at a rather low potential barrier of 2.32 V, followed by fast yet complete Li_2S dissociation to LiPS until 2.34 V in a charge depth of 47%. Afterward, the monoclinic and orthorhombic sulfur is formed at 2.47 V in a charge depth of 75%. The weak signals of sulfur imply the formation of less crystalline sulfur via strong chemical interaction with Co-C@MHF nanoreactors. As a contrast, the charge process of MXene and Co-free Li_2S@CHF is sluggish with 1.7-fold slower Li_2S dissociation rate, huge potential above 3.0 V, and delayed sulfur formation at 3.23 V via slow LiPS conversion. During cycling, no phase transition of fcc Co is observed in contour XRD pattern (fig. S38), suggesting that the Co acts as an actual active phase in electrocatalysis of Li_2S cathode. The presence of Co^0 not only facilitates the interfacial charge transport but also allows rapid LiPS adsorption and redox conversion on the same site without additional diffusion to the charge-assessable catalytic interface. In SPE, the activation and charge potential of Li_2S@Co-C@MHF are slightly increased to ca. 2.4 V together with fast and complete Li_2S dissociation. Weak sulfur signals appear in a charge depth as early as 18% before complete Li_2S dissociation, far sooner than the process in LEs. Formation of amorphous sulfur instead of crystalline phase is perhaps a result of the restricted LiPS diffusion and sulfur cluster migration in SPE. Such an amorphous phase with relatively lower formation energy and small domain size is favorable to reducing the redox difficulty of cathode reactions in SPE. The in operando electrochemical impedance spectroscopy (EIS) reveals an increment of the charge transfer resistance (R_{ct}) of Li_2S@Co-C@MHF in SPE in a charge depth of <45% (Fig. 6H and fig. S39), corresponding to Li_2S dissociation process (Fig. 6G). After that, the R_{ct} is back to a comparable level to those in LEs, suggesting a weak influence of SPE on LiPS conversion kinetics within highly conductive Co-C@MHF nanoreactor. The interfacial resistance (R_i) and system resistance (R_s) of the cells are reasonably higher but not so significant in SPE during charge. It can be attributed to the use of SPE with fast ionic transport and its superb interfacial contact to three-dimensional (3D) conductive networks of Co-C@MHF.

Strong chemical interaction of LiPS with Co-C@MHF also helps to regulate the Li_2S deposition behavior during discharge for optimizing the interfacial properties. The in operando XRD analysis

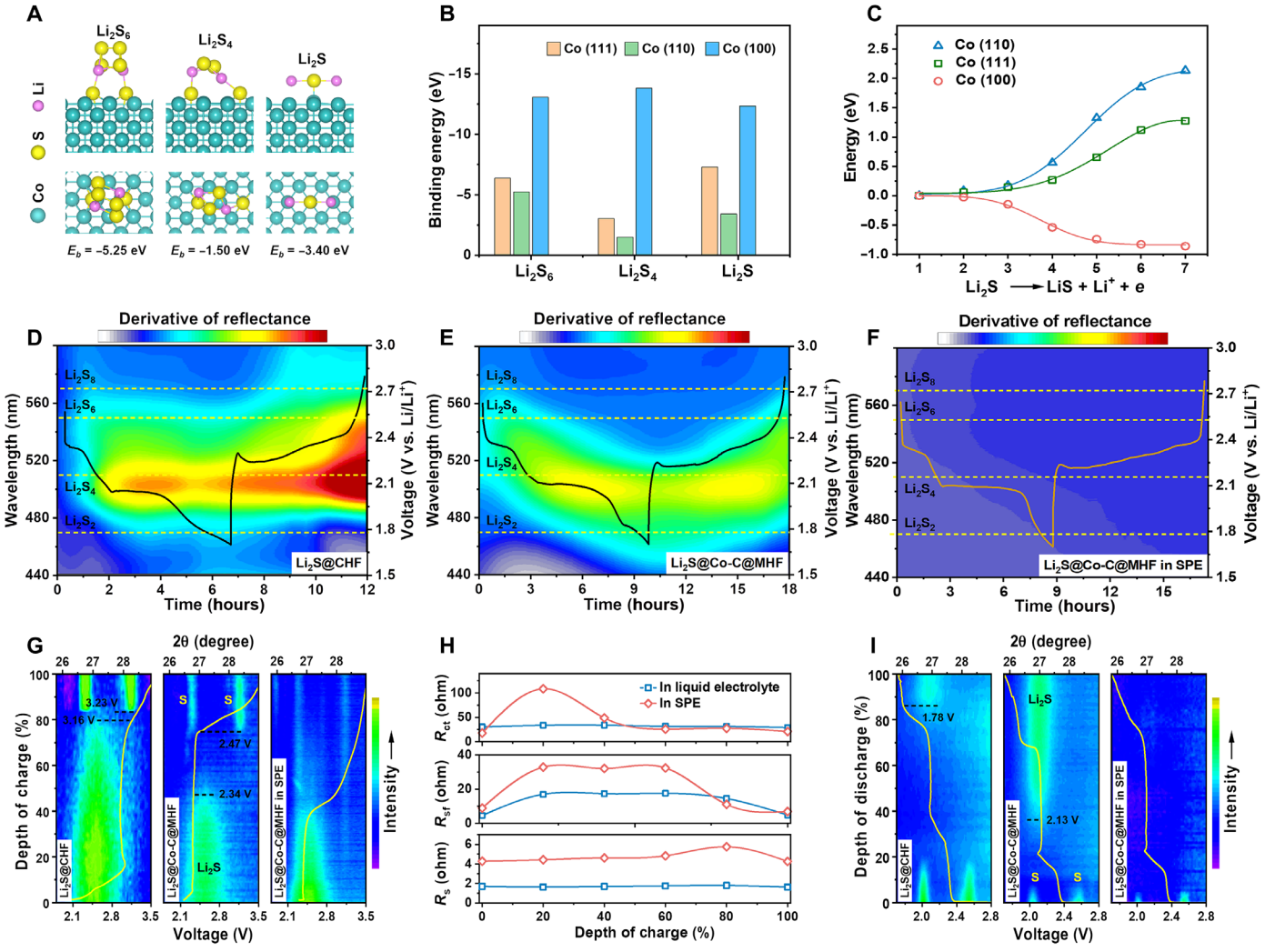

Fig. 6. Redox mechanism of Li_2S cathode in working cells. (**A**) Atomic structures of Li_2S, Li_2S_4, and Li_2S_6 molecules adsorbed on Co (110) plane. (**B**) Binding energy of these molecules and (**C**) energy profiles for Li_2S dissociation on different planes of Co. In operando ultraviolet-visible (UV-vis) contour patterns of (**D**) Li_2S@CHF and Li_2S@Co-C@MHF in (**E**) LEs or (**F**) SPE upon cycling. In operando XRD contour patterns of Li_2S@CHF (left), Li_2S@Co-C@MHF in LEs (middle) or SPE (right) during (**G**) charge and (**I**) discharge. (**H**) In operando EIS revealing the evolution of R_{ct}, R_{surf}, and R_s of Li_2S@Co-C@MHF with charge depth going in LEs and SPE.

reveals much faster Li_2S deposition on Co-C@MHF with rich chemically anchoring sites at a higher voltage (2.13 V) relative to CHF (1.78 V) (Fig. 6I). This observation is confirmed by the potentiostatic discharge test, where Li_2S nucleation on Co-C@MHF requires a shorter response time to achieve a higher current and deposition capacity (157.8 mAh g^{-1}) relative to CHF (101.6 mAh g^{-1}) (fig. S40). Efficient and uniform Li_2S deposition on Co-C@MHF contributes to not only electrode reversibility but also uniform cathode interface with low charge transfer resistance. In SPE, the Li_2S@Co-C@MHF exhibits a two-plateau discharge behavior, suggesting that the conversion of sulfur to Li_2S is still governed by a LiPS-intermediated pathway. Formation of Li_2S is identified by Li_2S nucleation overpotential in a discharge depth of 22.7%, as well as the similar discharge behavior in SPE and LEs. It is deposited on the electrode interface as an amorphous or cluster form without apparent XRD signals, possibly due to inhibited LiPS mobility in SPE, which is difficult to supply for Li_2S clusters to grow larger.

In summary, a rechargeable solid-state cell with high energy and safety is designed by mild yet energetic redox chemistry between Li_2S cathode and Si anode in SPE. A lack of extremely reactive cell components and robust cell configuration ensures high intrinsic cell safety with reduced hazardous exothermic side reactions. Remarkable reliability is achieved to enable reversible energy storage and output against thermal, electrical, or mechanical abuse in the ambient environment or even water. On this basis, a multilevel nanoreactor cathode design is applied to boost the redox activity and reversibility of Li_2S toward the sluggish charge. The Si anode is strengthened by sealing nanoparticulate Si in highly conductive MXene hollow shells. Both electrodes are glued in solid-state cells by in situ–polymerized SPE with fast ionic transport and LiPS impermeability for maximizing interfacial compatibility and cell robustness. A combination of various in operando analyses suggests that this solid-state cell undergoes a LiPS-intermediated multielectron redox pathway with amorphous final products in SPE free of LiPS

shuttling. Such energetic cell chemistry enables high specific energy for long-term cycling with negligible self-discharge and wide temperature adaptability besides high safety.

MATERIALS AND METHODS

Fabrication of Co-C@MHF fabric

The $Ti_3C_2T_x$ MXene (0.32 g) or ZIF-67 (0.3 g) was evenly dispersed in dimethylformamide (4 ml) containing PAN (M_w = 150,000, 0.396 g) or PMMA (M_w = 12,000, 1.33 g) as the sheath or core solution, respectively. Both solutions were applied for coaxial electrospinning to yield the fabric made of core-shelled polymer nanofibers. The fabric was annealed at 700°C with a ramp rate of 2°C min^{-1} for 2 hours in H_2/Ar flow to produce Co-C@MHF fabric. For comparison, the Co-free MHF, Co-C@CHF without MXene, and bare CHF were also fabricated similarly in the absence of ZIF-67, MXene, or both, respectively.

Fabrication of Li_2S@Co-C@MHF cathode

A mixture of Co-C@MHF and sulfur powder with a weight ratio of 1:1.3 was sealed in an Ar-filled stainless steel vessel and stored at 155°C for 18 hours. The product was immersed into 0.5 M lithium naphthalide in 1,2-dimethoxyethane (DME) for 2 hours to obtain Li_2S@Co-C@MHF. For comparison, the Li_2S@MHF, Li_2S@Co-C@CHF, and Li_2S@CHF cathodes were also fabricated similarly by using MHF, Co-C@CHF, or CHF for loading Li_2S, respectively.

Material characterization

The morphology of the samples was characterized by SEM (JSM-7800F, JEOL) and TEM (JEM-2100, JEOL and Tecnai G20, FEI) equipped with an energy dispersive spectrometer. The microstructure analysis of the samples was recorded by XRD (Cu Kα, D/MAX-2400, Rigaku). The texture of the samples was obtained by XPS (ESCALAB MK II, Thermo Fisher Scientific) with C 1s (284.6 eV) calibration. The weight ratio of sulfur in the electrode was measured by TGA (X70 equipment). The weight ratio of Li_2S was measured by ionic-coupled plasma optical emission spectroscopy (Optima 2000DV) and calibrated with electrode weight difference before and after loading Li_2S. The FTIR spectra were characterized by a Bruker EQUINOX 55 spectrophotometer. Raman spectra were obtained by a Horiba LabRAM HR Evolution Raman microscope. The infrared thermography of the pouch cells was measured by a thermal infrared camera (FLIR, C5).

Half-cell tests

The Li_2S@Co-C@MHF fabric was directly used as the working electrode against metallic Li foil as the counter and reference electrode. A solution of 1.0 M LiTFSI in DOL and DME (1:1 by volume) with 2.0 wt % $LiNO_3$ additive was used as the electrolyte. The mass loading of the cathodes is in a range of 2.0 to 6.0 mg cm^{-2} for different tests by layer-by-layer stacking of the fabrics. The ratio of electrolyte to Li_2S is 12 μl mg_{Li2S}^{-1}. Before the tests, the cells were galvanostatically charged to 3.5 V at 0.2 C (1 C = 1166 mA g^{-1}) to activate the Li_2S by a LAND CT2001A battery tester. Subsequent galvanostatic charge/discharge tests were conducted at various current rates between 1.7 and 2.8 V.

Assembly and tests of solid-state Li_2S||SPE||Si full cells

The Li_2S@Co-C@MHF and Si@MHF fabrics were directly used as the cathode and anode, respectively. The Si@MHF anodes were cycled for 2 cycles against Li in 1.0 M LiTFSI in DOL/DME as compensation for the initial irreversible capacity loss. The Li_2S loading in the cathode is 2.0 to 4.0 mg cm^{-2}, and the N/P ratio is fixed to ca. 1.2. An $Al(OTF)_3$/DOL solution (5 mM) was added into the cathode, which was diluted to 0.5 mM by adding LiTFSI/DOL solution (2 M) during cell assembling (*28*). The assembled cells were rested for at least 12 hours to accomplish the in situ polymerization of SPE. Celgard separators are used to avoid the electrode contact before SPE formation from the initially liquid electrolyte in the cells. The galvanostatic charge-discharge tests were carried out at 0.2 C between 1.2 and 2.8 V. The capacities of the full cells were limited by the cathode.

In operando characterization

The Li_2S@Co-C@MHF cathodes with 2.0 mg cm^{-2} Li_2S loading were used as the working electrode against metallic Li anode. The electrolyte is 1.0 M LiTFSI in DOL/DME (1:1 by volume) with 2.0 wt % $LiNO_3$ additive or SPE. In operando XRD analysis was performed on an x-ray powder diffractometer (D8 DISCOVER, Bruker) in a 2θ range of 5° to 70°, which was divided into three frames with an exposure time of 180 s for each frame. Meanwhile, the batteries were cycled between 1.7 and 3.5 V at 0.1 C by using a LAND CT2001A battery tester. In operando UV-vis tests were conducted by a UV-vis–near-infrared spectrometer (Lambda 750, PerkinElmer) equipped with a homemade battery module with a quartz window for UV reflection. The UV-vis spectra were collected per 10 min in a wavelength range of 300 to 700 nm during the galvanostatic cycle between 1.7 and 2.8 V at 0.1 C on a LAND CT2001A battery tester. In operando EIS measurements were performed on a Vertex.C.EIS electrochemical workstation (IVIUM). The EIS spectra were recorded per 60 min during cell running in a frequency range of 100 kHz to 10 mHz with an amplitude of 5 mV.

SUPPLEMENTARY MATERIALS

Supplementary material for this article is available at https://science.org/doi/10.1126/sciadv.abl8390

REFERENCES AND NOTES

1. Y. Fang, S. L. Zhang, Z.-P. Wu, D. Luan, X. W. Lou, A highly stable lithium metal anode enabled by Ag nanoparticle embedded nitrogen-doped carbon macroporous fibers. *Sci. Adv.* **7**, eabg3626 (2021).
2. A. Hu, W. Chen, X. Du, Y. Hu, T. Lei, H. Wang, L. Xue, Y. Li, H. Sun, Y. Yan, J. Long, C. Shu, J. Zhu, B. Li, X. Wang, J. Xiong, An artificial hybrid interphase for an ultrahigh-rate and practical lithium metal anode. *Energy Environ. Sci.* **14**, 4115–4124 (2021).
3. P. Albertus, S. Babinec, S. Litzelman, A. Newman, Status and challenges in enabling the lithium metal electrode for high-energy and low-cost rechargeable batteries. *Nat. Energy* **3**, 16–21 (2017).
4. J. Xiao, How lithium dendrites form in liquid batteries. *Science* **366**, 426–427 (2019).
5. X. Liu, D. Ren, H. Hsu, X. Feng, G.-L. Xu, M. Zhuang, H. Gao, L. Lu, X. Han, Z. Chu, J. Li, X. He, K. Amine, M. Ouyang, Thermal runaway of lithium-ion batteries without internal short circuit. *Joule* **2**, 2047–2064 (2018).
6. L. Zhang, T. Yang, C. Du, Q. Liu, Y. Tang, J. Zhao, B. Wang, T. Chen, Y. Sun, P. Jia, H. Li, L. Geng, J. Chen, H. Ye, Z. Wang, Y. Li, H. Sun, X. Li, Q. Dai, Y. Tang, Q. Peng, T. Shen, S. Zhang, T. Zhu, J. Huang, Lithium whisker growth and stress generation in an in situ atomic force microscope-environmental transmission electron microscope set-up. *Nat. Nanotechnol.* **15**, 94–98 (2020).
7. J. A. Lewis, F. J. Q. Cortes, Y. Liu, J. C. Miers, A. Verma, B. S. Vishnugopi, J. Tippens, D. Prakash, T. S. Marchese, S. Y. Han, C. Lee, P. P. Shetty, H.-W. Lee, P. Shevchenko, F. De Carlo, C. Saldana, P. P. Mukherjee, M. T. McDowell, Linking void and interphase evolution to electrochemistry in solid-state batteries using operando X-ray tomography. *Nat. Mater.* **20**, 503–510 (2021).
8. Y. Yu, J. Xie, H. Zhang, R. Qin, X. Liu, X. Lu, High-voltage rechargeable aqueous zinc-based batteries: Latest progress and future perspectives. *Small Sci.* **1**, 2000066 (2021).

9. Y. Xiao, K. Turcheniuk, A. Narla, A.-Y. Song, X. Ren, A. Magasinski, A. Jain, S. Huang, H. Lee, G. Yushin, Electrolyte melt infiltration for scalable manufacturing of inorganic all-solid-state lithium-ion batteries. *Nat. Mater.* **20**, 984–990 (2021).
10. M. Li, Z. Chen, T. Wu, J. Lu, Li_2S- or S-based lithium-ion batteries. *Adv. Mater.* **30**, 1801190 (2018).
11. Y. Yang, M. T. McDowell, A. Jackson, J. J. Cha, S. S. Hong, Y. Cui, New nanostructured Li_2S/silicon rechargeable battery with high specific energy. *Nano Lett.* **10**, 1486–1491 (2010).
12. J. Balach, T. Jaumann, L. Giebeler, Nanosized Li_2S-based cathodes derived from MoS_2 for high-energy density Li-S cells and Si-Li_2S full cells in carbonate-based electrolyte. *Energy Storage Mater.* **8**, 209–216 (2017).
13. Y. Shen, J. Zhang, Y. Pu, H. Wang, B. Wang, J. Qian, Y. Cao, F. Zhong, X. Ai, H. Yang, Effective chemical prelithiation strategy for building a silicon/sulfur li-ion battery. *ACS Energy Lett.* **4**, 1717–1724 (2019).
14. K. Zhang, L. Wang, Z. Hu, F. Cheng, J. Chen, Ultrasmall Li_2S nanoparticles anchored in graphene nanosheets for high-energy lithium-ion batteries. *Sci. Rep.* **4**, 6467 (2014).
15. Z. Wang, N. Zhang, M. Yu, J. Liu, S. Wang, J. Qiu, Boosting redox activity on MXene-induced multifunctional collaborative interface in high Li_2S loading cathode for high-energy Li-S and metallic Li-free rechargeable batteries. *J. Energy Chem.* **37**, 183–191 (2019).
16. J. Hassoun, B. Scrosati, A high-performance polymer tin sulfur lithium ion battery. *Angew. Chem. Int. Ed.* **49**, 2371–2374 (2010).
17. L. Wang, Y. Wang, Y. Xia, A high performance lithium-ion sulfur battery based on a Li_2S cathode using a dual-phase electrolyte. *Energy Environ. Sci.* **8**, 1551–1558 (2015).
18. Y. Fu, Z. Wu, Y. Yuan, P. Chen, L. Yu, L. Yuan, Q. Han, Y. Lan, W. Bai, E. Kan, C. Huang, X. Ouyang, X. Wang, J. Zhu, J. Lu, Switchable encapsulation of polysulfides in the transition between sulfur and lithium sulfide. *Nat. Commun.* **11**, 845 (2020).
19. T. Zhou, W. Lv, J. Li, G. Zhou, Y. Zhao, S. Fan, B. Liu, B. Li, F. Kang, Q.-H. Yang, Twinborn TiO_2-TiN heterostructures enabling smooth trapping-diffusion-conversion of polysulfides towards ultralong life lithium-sulfur batteries. *Energy Environ. Sci.* **10**, 1694–1703 (2017).
20. C. Zhao, G.-L. Xu, Z. Yu, L. Zhang, I. Hwang, Y.-X. Mo, Y. Ren, L. Cheng, C.-J. Sun, Y. Ren, X. Zuo, J.-T. Li, S.-G. Sun, K. Amine, T. Zhao, A high-energy and long-cycling lithium-sulfur pouch cell via a macroporous catalytic cathode with double-end binding sites. *Nat. Nanotechnol.* **16**, 166–173 (2020).
21. H. Shi, X. Ren, J. Lu, C. Dong, J. Liu, Q. Yang, J. Chen, Z. S. Wu, Dual-functional atomic zinc decorated hollow carbon nanoreactors for kinetically accelerated polysulfides conversion and dendrite free lithium sulfur batteries. *Adv. Energy Mater.* **10**, 2002271 (2020).
22. X. Meng, Y. Liu, Z. Wang, Y. Zhang, X. Wang, J. Qiu, A quasi-solid-state rechargeable cell with high energy and superior safety enabled by stable redox chemistry of Li_2S in gel electrolyte. *Energy Environ. Sci.* **14**, 2278–2290 (2021).
23. Y. Fang, D. Luan, S. Gao, X. W. Lou, Rational design and engineering of one-dimensional hollow nanostructures for efficient electrochemical energy storage. *Angew. Chem. Int. Ed.* **60**, 20102–20118 (2021).
24. Q. Pang, A. Shyamsunder, B. Narayanan, C. Y. Kwok, L. A. Curtiss, L. F. Nazar, Tuning the electrolyte network structure to invoke quasi-solid state sulfur conversion and suppress lithium dendrite formation in Li–S batteries. *Nat. Energy* **3**, 783–791 (2018).
25. X. Yang, J. Luo, X. Sun, Towards high-performance solid-state Li-S batteries: From fundamental understanding to engineering design. *Chem. Soc. Rev.* **49**, 2140–2195 (2020).
26. G. Zhou, H. Tian, Y. Jin, X. Tao, B. Liu, R. Zhang, Z. W. Seh, D. Zhuo, Y. Liu, J. Sun, J. Zhao, C. Zu, D. S. Wu, Q. Zhang, Y. Cui, Catalytic oxidation of Li_2S on the surface of metal sulfides for Li-S batteries. *Proc. Natl. Acad. Sci.* **114**, 840–845 (2017).
27. L.-Z. Fan, H. He, C.-W. Nan, Tailoring inorganic–polymer composites for the mass production of solid-state batteries. *Nat. Rev. Mater.* **6**, 1003–1019 (2021).
28. Q. Zhao, X. Liu, S. Stalin, K. Khan, L. A. Archer, Solid-state polymer electrolytes with in-built fast interfacial transport for secondary lithium batteries. *Nat. Energy* **4**, 365–373 (2019).
29. R. Wang, J. Yang, X. Chen, Y. Zhao, W. Zhao, G. Qian, S. Li, Y. Xiao, H. Chen, Y. Ye, G. Zhou, F. Pan, Highly dispersed cobalt clusters in nitrogen-doped porous carbon enable multiple effects for high-performance Li-S Battery. *Adv. Energy Mater.* **10**, 1903550 (2020).
30. M. Li, J. Lu, J. Shi, S.-B. Son, D. Luo, I. Bloom, Z. Chen, K. Amine, In situ localized polysulfide injector for the activation of bulk lithium sulfide. *J. Am. Chem. Soc.* **143**, 2185–2189 (2021).
31. K. Cai, M.-K. Song, E. J. Cairns, Y. Zhang, Nanostructured Li_2S–C composites as cathode material for high-energy lithium/sulfur batteries. *Nano Lett.* **12**, 6474–6479 (2012).
32. J. Zhang, Y. Shi, Y. Ding, L. Peng, W. Zhang, G. Yu, A conductive molecular framework derived Li_2S/N,P-codoped carbon cathode for advanced lithium-sulfur batteries. *Adv. Energy Mater.* **7**, 1602876 (2017).
33. F. Wu, J. T. Lee, N. Nitta, H. Kim, O. Borodin, G. Yushin, Lithium iodide as a promising electrolyte additive for lithium-sulfur batteries: Mechanisms of performance enhancement. *Adv. Mater.* **27**, 101–108 (2015).
34. M. Li, Z. Bai, Y. Li, L. Ma, A. Dai, X. Wang, D. Luo, T. Wu, P. Liu, L. Yang, K. Amine, Z. Chen, J. Lu, Electrochemically primed functional redox mediator generator from the decomposition of solid state electrolyte. *Nat. Commun.* **10**, 1890 (2019).
35. G. Tan, R. Xu, Z. Xing, Y. Yuan, J. Lu, J. Wen, C. Liu, L. Ma, C. Zhan, Q. Liu, T. Wu, Z. Jian, R. Shahbazian-Yassar, Y. Ren, D. J. Miller, L. A. Curtiss, X. Ji, K. Amine, Burning lithium in CS_2 for high-performing compact Li_2S-graphene nanocapsules for Li-S batteries. *Nat. Energy* **2**, 17090 (2017).
36. M. Yu, S. Zhou, Z. Wang, W. Pei, X. Liu, C. Liu, C. Yan, X. Meng, S. Wang, J. Zhao, J. Qiu, A molecular-cage strategy enabling efficient chemisorption-electrocatalytic interface in nanostructured Li_2S cathode for li metal-free rechargeable cells with high energy. *Adv. Funct. Mater.* **29**, 1905986 (2019).
37. Z. W. Seh, J. H. Yu, W. Li, P.-C. Hsu, H. Wang, Y. Sun, H. Yao, Q. Zhang, Y. Cui, Two-dimensional layered transition metal disulphides for effective encapsulation of high-capacity lithium sulphide cathodes. *Nat. Commun.* **5**, 5017 (2014).
38. A. Hu, M. Zhou, T. Lei, Y. Hu, X. Du, C. Gong, C. Shu, J. Long, J. Zhu, W. Chen, X. Wang, J. Xiong, Optimizing redox reactions in aprotic lithium–sulfur batteries. *Adv. Energy Mater.* **10**, 2002180 (2020).
39. S. S. Zhang, A new finding on the role of $LiNO_3$ in lithium-sulfur battery. *J. Power Sources* **322**, 99–105 (2016).
40. L. Ma, S. Chen, X. Li, A. Chen, B. Dong, C. Zhi, Liquid-free all-solid-state zinc batteries and encapsulation-free flexible batteries enabled by in situ constructed polymer electrolyte. *Angew. Chem. Int. Ed.* **59**, 23836–23844 (2020).
41. F. Shahzad, A. Iqbal, H. Kim, C. M. Koo, 2D Transition metal carbides (MXenes): Applications as an electrically conducting material. *Adv. Mater.* **32**, 2002159 (2020).
42. G. G. Eshetu, X. Judez, C. Li, M. Martinez-Ibañez, I. Gracia, O. Bondarchuk, J. Carrasco, L. M. Rodriguez-Martinez, H. Zhang, M. Armand, Ultrahigh performance all solid-state lithium sulfur batteries: Salt anion's chemistry-induced anomalous synergistic effect. *J. Am. Chem. Soc.* **140**, 9921–9933 (2018).
43. Y. X. Song, Y. Shi, J. Wan, S.-Y. Lang, X.-C. Hu, H.-J. Yan, B. Liu, Y.-G. Guo, R. Wen, L.-J. Wan, Direct tracking of the polysulfide shuttling and interfacial evolution in all-solid-state lithium–sulfur batteries: A degradation mechanism study. *Energy Environ. Sci.* **12**, 2496–2506 (2019).
44. H. Jha, I. Buchberger, X. Cui, S. Meini, H. A. Gasteiger, Li-S batteries with Li_2S cathodes and Si/C anodes. *J. Electrochem. Soc.* **162**, A1829–A1835 (2015).
45. Z. Hao, J. Chen, L. Yuan, Q. Bing, J. Liu, W. Chen, Z. Li, F. R. Wang, Y. Huang, Advanced Li_2S/Si full battery enabled by tin polysulfide immobilizer. *Small* **15**, 1902377 (2019).
46. S. Wang, H. Chen, Z. Zhong, X. Hou, S. Hu, J. Wu, Graphene-decorated sphere Li_2S composite prepared by spray drying method as cathode for lithium-sulfur full cell. *Ionics* **24**, 3385–3392 (2018).
47. M. Agostini, J. Hassoun, J. Liu, M. Jeong, H. Nara, T. Momma, T. Osaka, Y.-K. Sun, B. Scrosati, A lithium-ion sulfur battery based on a carbon-coated lithium-sulfide cathode and an electrodeposited silicon-based anode. *ACS Appl. Mater. Interfaces* **6**, 10924–10928 (2014).
48. J. Wu, Z. Rao, Z. Cheng, L. Yuan, Z. Li, Y. Huang, Ultrathin, flexible polymer electrolyte for cost-effective fabrication of all-solid-state lithium metal batteries. *Adv. Energy Mater.* **9**, 1902767 (2019).
49. Q. Ma, J. Yue, M. Fan, S.-J. Tan, J. Zhang, W.-P. Wang, Y. Liu, Y.-F. Tian, Q. Xu, Y.-X. Yin, Y. You, A. Luo, S. Xin, X.-W. Wu, Y.-G. Guo, Formulating the electrolyte towards high-energy and safe rechargeable lithium-metal batteries. *Angew. Chem. Int. Ed.* **60**, 16554–16560 (2021).
50. Z. Chen, X. Li, D. Wang, Q. Yang, L. Ma, Z. Huang, G. Liang, A. Chen, Y. Guo, B. Dong, X. Huang, C. Yang, C. Zhi, Grafted MXene/polymer electrolyte for high performance solid zinc batteries with enhanced shelf life at low/high temperatures. *Energy Environ. Sci.* **14**, 3492–3501 (2021).
51. Y.-G. Lee, S. Fujiki, C. Jung, N. Suzuki, N. Yashiro, R. Omoda, D.-S. Ko, T. Shiratsuchi, T. Sugimoto, S. Ryu, J. H. Ku, T. Watanabe, Y. Park, Y. Aihara, D. Im, I. T. Han, High-energy long-cycling all-solid-state lithium metal batteries enabled by silver–carbon composite anodes. *Nat. Energy* **5**, 299–308 (2020).
52. R. Xu, J. Yue, S. Liu, J. Tu, F. Han, P. Liu, C. Wang, Cathode-supported all-solid-state lithium–sulfur batteries with high cell-level energy density. *ACS Energy Lett.* **4**, 1073–1079 (2019).
53. D. Wang, Y. Wu, X. Zheng, S. Tang, Z. Gong, Y. Yang, Li_2S@NC composite enable high active material loading and high Li_2S utilization for all-solid-state lithium sulfur batteries. *J. Power Sources* **479**, 228792 (2020).
54. W. Liu, C. Yi, L. Li, S. Liu, Q. Gui, D. Ba, Y. Li, D. Peng, J. Liu, Designing polymer-in-salt electrolyte and fully infiltrated 3d electrode for integrated solid-state lithium batteries. *Angew. Chem. Int. Ed.* **60**, 12931–12940 (2021).
55. R. Bouchet, S. Maria, R. Meziane, A. Aboulaich, L. Lienafa, J.-P. Bonnet, T. N. T. Phan, D. Bertin, D. Gigmes, D. Devaux, R. Denoyel, M. Armand, Single-ion BAB triblock copolymers as highly efficient electrolytes for lithium-metal batteries. *Nat. Mater.* **12**, 452–457 (2013).

56. D. R. Deng, F. Xue, C.-D. Bai, J. Lei, R. Yuan, M. S. Zheng, Q. F. Dong, Enhanced adsorptions to polysulfides on graphene-supported bn nanosheets with excellent li-s battery performance in a wide temperature range. *ACS Nano* **12**, 11120–11129 (2018).
57. S.-H. Chung, A. Manthiram, Lithium–sulfur batteries with the lowest self-discharge and the longest shelf life. *ACS Energy Lett.* **2**, 1056–1061 (2017).
58. W. Cai, C. Yan, Y.-X. Yao, L. Xu, X.-R. Chen, J.-Q. Huang, Q. Zhang, The boundary of lithium plating in graphite electrode for safe lithium-ion batteries. *Angew. Chem. Int. Ed.* **60**, 13007–13012 (2021).
59. H. Wang, Y. Shao, H. Pan, X. Feng, Y. Chen, Y.-S. Liu, E. D. Walter, M. H. Engelhard, K. S. Han, T. Deng, G. Ren, D. Lu, X. Lu, W. Xu, C. Wang, J. Feng, K. T. Mueller, J. Guo, K. R. Zavadil, J.-G. Zhang, A lithium-sulfur battery with a solution-mediated pathway operating under lean electrolyte conditions. *Nano Energy* **76**, 105041 (2020).
60. X. Liang, Y. Rangom, C. Y. Kwok, Q. Pang, L. F. Nazar, Interwoven MXene nanosheet/carbon-nanotube composites as Li-S cathode hosts. *Adv. Mater.* **29**, 1603040 (2017).

Acknowledgments

Funding: This work was supported by the National Natural Science Foundation of China (NSFC, nos. 51772040 and 51972040), Talent Program of Rejuvenation of the Liaoning (no. XLYC1807032), Innovation Support Program for High-level Personnel Recruitment of Dalian City (no. 2018RJ04), and Fundamental Research Funds for the Central Universities (no. DUT20TD203). **Author contributions**: Z.W., J.Q., and Y.L. conceived the idea and co-wrote the manuscript. Y.L. and X.M. performed the experiments and theoretical calculations. Z.W. and J.Q. guided all aspects of the work. **Competing interests:** The authors declare that they have no competing interests. **Data and materials availability:** All data needed to evaluate the conclusions in the paper are present in the paper and/or the Supplementary Materials.

Submitted 9 August 2021
Accepted 12 November 2021
Published 5 January 2022
10.1126/sciadv.abl8390

ScienceAdvances

A Li2S-based all-solid-state battery with high energy and superior safety

Yuzhao LiuXiangyu MengZhiyu WangJieshan Qiu

Sci. Adv., 8 (1), eabl8390. • DOI: 10.1126/sciadv.abl8390

Science Advances (ISSN) is published by the American Association for the Advancement of Science. 1200 New York Avenue NW, Washington, DC 20005. The title *Science Advances* is a registered trademark of AAAS.